High temperature oxidation treated 3D printed anatomical WE43 alloy scaffolds for repairing periarticular bone defects: *In vitro* and *in vivo* studies

Bingchuan Liu [a,b,1], Jinge Liu [c,d,1], Chaoxin Wang [a,b], Zhengguang Wang [a,b], Shuyuan Min [a,b], Caimei Wang [e], Yufeng Zheng [f,*], Peng Wen [c,d,**], Yun Tian [a,b,***]

[a] Department of Orthopaedics, Peking University Third Hospital, Beijing, 100191, China
[b] Engineering Research Center of Bone and Joint Precision Medicine, Ministry of Education, Beijing, 100191, China
[c] The State Key Laboratory of Tribology, Tsinghua University, Beijing, 100084, China
[d] Department of Mechanical Engineering, Tsinghua University, Beijing, 100084, China
[e] Beijing AKEC Medical Co., Ltd., Beijing, 102200, China
[f] School of Materials Science and Engineering, Peking University, Beijing, 100871, China

ARTICLE INFO

ABSTRACT

Reconstruction of subarticular bone defects is an intractable challenge in orthopedics. The simultaneous repair of cancellous defects, fractures, and cartilage damage is an ideal surgical outcome. 3D printed porous anatomical WE43 (magnesium with 4 wt% yttrium and 3 wt% rare earths) scaffolds have many advantages for repairing such bone defects, including good biocompatibility, appropriate mechanical strength, customizable shape and structure, and biodegradability. In a previous investigation, we successfully enhanced the corrosion resistance of WE43 samples via high temperature oxidation (HTO). In the present study, we explored the feasibility and effectiveness of HTO-treated 3D printed porous anatomical WE43 scaffolds for repairing the cancellous bone defects accompanied by split fractures via in vitro and *in vivo* experiments. After HTO treatment, a dense oxidation layer mainly composed of Y_2O_3 and Nd_2O_3 formed on the surface of scaffolds. In addition, the majority of the grains were equiaxed, with an average grain size of 7.4 μm. Cell and rabbit experiments confirmed the non-cytotoxicity and biocompatibility of the HTO-treated WE43 scaffolds. After the implantation of scaffolds inside bone defects, their porous structures could be maintained for more than 12 weeks without penetration and for more than 6 weeks with penetration. During the postoperative follow-up period for up to 48 weeks, radiographic examinations and histological analysis revealed that abundant bone gradually regenerated along with scaffold degradation, and stable osseointegration formed between new bone and scaffold residues. MRI images further demonstrated no evidence of any obvious damage to the cartilage, ligaments, or menisci, confirming the absence of traumatic osteoarthritis. Moreover, finite element analysis and biomechanical tests further verified that the scaffolds was conducive to a uniform mechanical distribution. In conclusion, applying the HTO-treated 3D printed porous anatomical WE43 scaffolds exhibited favorable repairing effects for subarticular cancellous bone defects, possessing great potential for clinical application.

1. Introduction

Severe periarticular limb fractures are frequently associated with articular surface subsidence and cancellous bone compression. Segmental cancellous bone defects will arise in the subarticular areas after surgical reduction, causing great clinical treatment challenges [1, 2]. Although bone defects exhibit self-healing abilities, large irregular defects cannot heal by themselves if left untreated. These bone defects were characterized by irregular anisotropy in both contour morphology and structures, accompanied with local complex compositions and

mechanical environment. Besides, these bone defects are located at the load-bearing area of the joints, which puts forward higher requirements for their mechanical strength after repair. Improper repair will cause the articular surface to lose effective support and collapse, and in serious cases, a secondary revision operation is needed, increasing the pain and burden of patients.

An effective method to rapidly restore the physiological function of defective bone tissue involves the use of appropriate bone graft materials. For these subarticular cancellous defects, traditional filling materials include allografts, autografts, xenografts, and artificial bones, which can play a role in space occupation and osteoinduction. Unfortunately, the mechanical strength of these traditional materials is relatively weak, and their unconsolidated accumulation status and excessive degradation rate make it difficult for them to offer enduring and stable mechanical support for reduced articular fractures. Under these circumstances, stress conducts mainly along the plates and screws, resulting in a higher risk of screw breakage and fracture re-collapse. Some new types of bone substitutes have been reported in previous studies, such as hydrogel [3], gelatin, bioactive glass [4], and some synthetic polymer materials [5]. These innvative mateirals displayed good biocompatibility and osteoinductivity, but their elastic modulus was far different from that of bone, and they could not meet the needs of repairing irregular bone defects. An ideal bone substitute must exhibit good biological compatibility, appropriate mechanical strength close to natural bone, structures with interconnected pores, and good biodegradability and secondary products [6].

In recent decades, advances have been made in the development of metallic bone substitutes, particularly, titanium (Ti) alloys. 3D printed Ti-alloy prostheses have been employed for clinically repairing bone defects and have achieved favorable effects, as demonstrated in our previous research [7–9]. Compared to traditional bone-repair materials, the outstanding advantages of these prostheses lie in customizable structures and sufficient mechanical strength. However, the non-biodegradable property of Ti-alloy prostheses makes them unsuitable for some clinical situations, such as cancellous bone defects secondary to periarticular fractures. The eternal existence of Ti-alloy prostheses produces local occupying and stress-shielding effects, thereby affecting the autonomous growth and reconstruction of cancellous bone.

In contrast, bone substitutes manufactured by magnesium (Mg) alloys are more applicable for repairing periarticular cancellous bone defects. Mg alloys have been recognized as green engineering materials since the twenty-first century. The density of Mg is about 1.7 g/cm^3 and Young's modulus is equal to 42 GPa, being very similar to those of human bone (which has a density of 1.95 g/cm^3 and Young's modulus of 3–20 GPa) [6]. Mg alloys also have outstanding properties such as desirable biocompatibility and biodegradability [10,11]. Furthermore, degradable Mg-based implants do not require a second surgery to be removed from the body, thus avoiding additional pain and financial burdens. WE43 (4% Yttrium (Y), 3% (Neodymium + Gadolinium) (Nd + Gd), 0.5% Zirconium (Zr), and remaining Mg, in mass) is one of the few Mg alloys that have been clinically applied to date. In 2013 and 2016, the WE43 screws and vascular stents from Syntellix® *and Magnezix® were certified by CE, respectively [12,13]. Based on this, 3D printing technology can be used to develop highly complex geometries for manufacturing WE43 implants based on a computer-aided designing program, further amplifying the intrinsic advantages of WE43 alloys, and making them more suitable for the complex anatomical morphology and biomechanical environment around the joints.*

In our preliminary work, we achieved high-quality 3D printed porous WE43 scaffolds [14], and confirmed their credible biocompatibility and osteoinduction. In addition, we successfully improved the corrosion resistance of the printed WE43 samples via high temperature oxidation (HTO) method. The HTO-treated samples were able to maintain their structural integrity and lost only 6.88% weight after a 28-day immersion in Hank's solution [15]. In theory, this kind of HTO-treated and customized WE43 scaffold has emerged as a promising choice for repairing irregular periarticular cancellous bone defects. After implantation, the dynamic process from the initial morphological and mechanical match to the gradual scaffold degradation and new bone regeneration is expected to assist in achieving "complete reconstruction" of defects, which fulfills the mission of promoting the healing process and then degrades completely with no residues [16,17].

In this study, we systematically explored the efficacy of HTO-treated 3D printed porous anatomical WE43 scaffolds for repairing cancellous bone defects accompanied by periarticular fractures. Our focus was on determinin (1) the cytotoxicity and biocompatibility of HTO-treated WE43 scaffolds, (2) the dynamic behaviors of scaffold degradation and new bone regeneration, and (3) the biomechanical characteristics of different fixation modes. Using in vitro cell cultures, finite element analysis (FEA), biomechanical tests, and *in vivo* 48-week-long rabbit experiments, we fully illustrated the feasibility and effectiveness of these scaffolds in repairing subarticular cancellous defects. Our results provide an important foundation for future clinical trials.

2. Materials and methods

2.1. Fabrication of 3D printed WE43 scaffolds and HTO treatment

*The commercial WE43 magnesium alloy powders (*Tangshan Weihao, China*) prepared by plasma rotation electrode process (PREP) were used with an average size of 42.*42 μm *and were composed of 3.87 wt% Y, 2.24 wt% Nd, 1.16 wt% Gd, 0.39 wt% Zr and residual Mg. The L-PBF system (BLT S210, China) employed a ytterbium fiber laser (IPG YLR-500, Germany) with a diameter of 70 μm. The laser power was 60 W, and the scanning speed was 600 mm/s. The layer thickness was 20 μm. A zig-zag scanning strategy with the hatching distance of 70 μm and rotation angle of 70o was employed to inner region of the scaffold. Before the L-PBF, the printing platform was preheated to 200 °C, and the oxygen content was kept below 100 ppm by the circular high purity argon (99.99%).* More technical details regarding the LPBF fabrication and quality process were shown in our previous report [14]. The scaffolds for compression tests were cylindrical with a size of $\varphi 10 \times 10$ mm. The scaffolds for *in vivo* implantation tests were designed based on the femur CT data of experimental rabbits with an external size of $14 \times 7 \times 7$ mm, which simulated the natural anatomical morphology of the distal femur (Supplementary Figure A). The internal frame was set as porous gyroid structures, with a porosity of 60%, and a strut size of 450 μm.

After LPBF, the scaffolds were chemically polished in the solution containing 5% HCl, 5% HNO_3, and balanced C_2H_5OH for 120 s. Subsequently, HTO process was performed in a muffle furnace (HF-Kejing KSL-1200, China) with circulating air. The process parameters of HTO have been optimized based on our previous research [15]. The scaffolds were heated to 525 °C for 8 h with a heating rate of 10 °C/min, then the scaffolds were quenched in the water at room temperature. The scaffolds were heated to 525 °C for 8 h with a heating rate of 10 °C/min, then the scaffolds were quenched in the water at room temperature. After HTO, the scaffolds were sterilized with ethylene oxide and individually packaged.

2.2. Surface and microstructure characterization

The microstructure of the scaffolds with HTO was analyzed by scanning electron microscopy (SEM, Zeiss Gemini-300, Germany) equipped with energy dispersive X-ray spectroscopy (EDS), backscatter electron detector (BSE), and electron backscatter diffraction (EBSD). The BSE and EDS analysis used a working voltage of 10 kV. While, EBSD used a working voltage of 25 kV. The microstructure was observed at $400\times$ and $3000\times$. The phase composition was characterized via Xray diffraction (XRD, Bruker D-8, USA) with the scanning range and step size of 20o $\sim$ 80o and 0.02o, respectively.

2.3. Mechanical strength

Compression tests of the scaffolds were conducted using a universal tester (Instron 5565, UK) with a rate of 1 mm/min. The ultimate strength, yield strength, and Young's modulus were calculated. The full-field maximum technical strain of the scaffolds during the compressive process was recorded by a digital image correlation (DIC, XTOP CONST-5M, China).

2.4. Cell experiments

In vitro cell experiments were performed with MC3T3-E1 murine osteoblasts (MC cells) in a medium containing scaffold extracts to assess the effect on cell proliferation and differentiation, and the ability to promote osteoinductive protein secretion of the HTO-treated scaffolds.

2.4.1. Preparation of scaffold extracts

The medium used for extract preparation and cell culture was Dulbecco's Modified Eagle Medium (DMEM, Gibco, USA) containing 10% fetal bovine serum and 100 U/mL penicillin-streptomycin combination. First, the scaffolds were soaked in DMEM medium for 24 h at 37 °C to obtain an extract with a ratio of 4 cm^2/mL. Subsequently, the soaking solution was centrifuged, and the supernatant was collected as a 100% extract. We then mixed the 100% extract with an appropriate amount of DMEM to prepare a 50% scaffold extract.

2.4.2. Cytotoxicity

MC cells were cultured in DMEM medium at 37 °C, 5% CO$_2$, and saturated humidity in a constant temperature incubator. The medium was changed every 2 days, and the cells were subcultured when they reached 90% fullness. MC cells were seeded on 48-well plates (Corning, USA) with 1×10^4 cells per well, 300 μL per well. The cells were allowed to grow for 24 h to achieve adhesion. According to the different experimental groups, the extracts at concentrations of 0%, 50%, and 100% were added, and the cells continued to be cultured for 1, 3, and 7 days. The cytotoxicity of different extract concentrations was evaluated using Live/Dead assays. At different time nodes, the plates were washed with phosphate-buffered saline (PBS), and each well was injected with 130 μL working solution, which was configurated by adding 4 μL EthD-1 and 1 μL Ca-AM inside 10 mL D-PBS solution. The samples were then incubated with the working solution for 15 min in the dark. The status of the acquired cells was observed using a fluorescent microscope (living cells were green and dead cells were red). Cell Counting Kit-8 (CCK-8) assays were also implemented at the corresponding time nodes, during which 100 μL CCK-8 reagent (Solarbio, China) was added inside each well. The percentage of viable cells was quantitatively recorded.

2.4.3. Western blot analysis

Western blot analysis was performed to determine the protein secretion levels of osteocalcin (OCN) and osteopontin (OPN) in a medium. First, the samples were centrifuged and the protein concentration of the supernatant was determined using a BCA kit (Solarbio, China). The separated proteins were then transferred onto polyvinylidene fluoride membranes. The membranes were blocked using 5% fat-free dry milk for 2 h, followed by incubation with the primary antibodies including anti-rat anti-OCN, anti-OPN, and anti-β-actin polyclonal antibodies at 4 °C overnight. Membranes were washed with Tris Buffered Saline with Tween (TBST) solution and incubated with the corresponding secondary antibodies for 1 h at room temperature. The samples were washed again with TBST. The results were visualized using an ECL detection kit, and an automatic chemiluminescence image analysis system was used for exposure. Image J software was used to analyze the grey values of different protein bands.

2.5. Finite element analysis

Before implementing the *in vivo* animal experiments, we used finite element analysis (FEA) to stimulate and compare the effects of different repair materials and internal fixation modes for subarticular cancellous defects accompanied by split fractures in the distal femur. FEA could demonstrate the biomechanical distribution and concentration of the skeletal tissues and implants. As shown in Supplementary Figure B, the FEA model comprised the fracture fragment, femoral shaft, screws, plate, scaffold, and cement particles. We established a model of a lateral split fracture accompanied by cancellous bone defects. Four models were set up: Blank model (defects were left blank), Cement model (defects were filled with incompact cement particles), Scaffold I and II models (defects were filled with anatomical WE43 scaffolds). The difference between the latter two models was that part of the screws in Scaffold I penetrated the scaffolds, while the screws in Scaffold II avoided penetration. The elastic moduli of bone, plate, screw, cement, and scaffold were assigned values of 16,600 MPa, 110,000 MPa, 110,000 MPa, 3000 MPa, and 30,230 MPa, respectively. The Poisson's ratio of all the materials was set as 0.3. While applying the press, the proximal end of the femur was fixed, and the presses were applied separately from the unilateral or overall directions. The pressure was set at 50 N. We recorded and compared the von Mises values of the fracture fragment, femoral shaft, screws, plate, and scaffold.

2.6. Animal experiments

2.6.1. Grouping, building models, and harvesting specimens

The experimental rabbits were supplied and fed by the Department of Laboratory Animal Science of Peking University Health Science Center. Animal management, surgical protocols, and welfare were carried out in accordance with the guidelines of Good Laboratory Practices regulation and were approved by the Ethical Committee of Laboratory Animal Science Research (No. A2020404). A total of 96 male New Zealand white rabbits (weighing from 2.5 to 3.0 kg) were enrolled, and their left back legs were selected for our experiment. The experimental model used in this study was a unilateral split femoral condylar fracture accompanied by a subarticular cancellous bone defect, which has not been reported previously. This model is consistent with the real trauma type observed in the clinic, equivalent to a type-B fracture based on the classical AO classification system [18]. This model could fully evaluate the effects and clinical application prospects of the experimental scaffolds. Similar to the FEA model, all enrolled rabbits were divided into four groups, including the Blank group (defects were left blank), Cement group (defects were filled with cement particles), Scaffold I and II groups (defects were filled with printed porous anatomical WE43 scaffolds). Commercial bone cement (Wright Medical Technology, Inc., USA) consisted of calcium sulfate. Each group contained the same number of 24 rabbits.

Before surgery, all rabbits were acclimated for 2 weeks to confirm their health and normal patellofemoral joint movement. Supplementary Figure C shows the entire surgical process used to construct our model. General anesthesia was administered using ketamine hydrochloride (50 mg/kg, IM) and fentanyl (0.17 mg/kg, IM). First, the femoral condyle was fully exposed after patella dislocation. The lateral condyle was cut using a chainsaw to form a split fracture. Subsequently, the lateral fracture fragment was pried open, and a part of the subarticular cancellous bone was scraped with a spoon to create an obvious defect. According to the different experimental groups, the cancellous bone defects were respectively left blank or filled with cement particles and scaffolds. Finally, the fracture fragment was restored using a clamp, and a plate and screws were applied for internal fixation. In the Cement group, the screws penetrated the cement particles. We also penetrated the scaffolds using partial screws in the Scaffold I group, while avoiding penetration in the Scaffold II group. The patella was repositioned, and the incision was closed layer by layer. All rabbits were housed in

separate cages and allowed unlimited activity. During the early five days after surgery, the intramuscular antibiotics (0.2 g/kg cefazolin sodium) were injected to prevent potential infection. During the follow-up periods, a certain number of rabbits were euthanized, and their leg specimens were removed for further experiments: six specimens were harvested at 6, 12, 24, and 48 weeks from each group, and timely replacement would be completed once unexpected failure or death occurred. During the process of collecting specimens, the soft tissue surrounding the femur and tibia would be stripped, but the integrity of the ligaments around the knees were preserved.

2.6.2. Gross observation

During the breeding process, the status of rabbits' overall health and surgical site received constant attention; their mental attitude, appetite, range of leg motion, and wound recovery were observed. After harvesting, the specimens were carefully examined for infection, necrosis, and implant displacement.

2.6.3 X-ray, Micro-computed-tomography and magnetic resonance imaging examinations.

Continuous radiological examinations were performed using a C-arm fluoroscope and an INVEON Micro-computed-tomography (Micro-CT) scanner (Siemens, Germany). X-rays provided important information regarding the stability of screws and scaffolds, scaffold degradation, new bone growth, fracture healing, and possible complications. Micro-CT images could exhibit more detailed evidence about the degradation and regeneration processes of scaffolds and new bones. Magnetic resonance imaging (MRI) examination was performed by a nuclear magnetic resonance instrument (Siemens, Germany), and the images were used to observe the degeneration degree of the ligaments, cartilage, and menisci, as well as the occurrence of traumatic osteoarthritis. Furthermore, we used the magnetic resonance observation of cartilage repair tissue (MOCART) score scale to quantitatively assess cartilage degeneration. The total score of the MOCART scale was 100 and covered nine scoring indicators, including the degree of defect repair and filling of the defect, integration to the border zone, the surface of the repair tissue, structure of the repair tissue, the signal intensity of the repair tissue, subchondral lamina, subchondral bone, adhesions, and effusion [19].

2.6.3. Histological analysis

Following the image logical examinations, specimens were fixed in paraformaldehyde at room temperature for three days. They were then embedded and sliced into 200 μm sections and grounded to 20–30 μm by a sliding microtome (EXAKT, Germany). Methylene blue/acid fuchsin staining was used to observe the scaffold degradation and new bone regeneration (black and grey materials represent the scaffold and its residuum, pink tissue represents the newly-regenerated bone, and blue tissue represents osteoblasts and the surrounding cellular matrix).

2.6.4. Biomechanical experiments

At each time point, three of the harvested specimens from each group were used to perform in vitro biomechanical experiments, which were fulfilled via the Microtensile torque test system (E1000, Instron, USA) and WaveMatrix dynamic recording software (USA). Each specimen was vertically fixed on the operating table. After that, a vertical load was applied to the distal surface at a rate of 2 mm/min until refracture occurred. Then, we drew a load-displacement curve based on the recorded data and recognized the maximum bearing load through the inflection point of the curve.

2.7. Statistical analysis

Statistical analysis was completed via SPSS 20.0 software. Differences with respect to the cell viability percentage from the CCK-8 assay, the osteoinductive protein secretion level from Western blot analysis, maximum bearing load from the in vitro biomechanical experiment and MOCART scores were compared using a Student's t-test. $P < 0.05$ was

defined as statistically significant. All results were shown in the form of bar graph.

3. Results

3.1. Characterizations of microstructure, element distribution, and mechanical strength

Fig. 1 showed the microstructure and phase composition analysis of the porous scaffolds with HTO treatment. The cross section of scaffold exhibited a sandwich structure at the surface, as shown in Fig. 1A. The surface of scaffold was covered by a dense and continuous film with a thickness of about 2 μm. The layer exhibited an enrichment of elements O, Y, Nd, Gd, and Zr based on the EDS mapping result (Fig. 1B). In addition, Y_2O_3 and Nd_2O_3 were detected at the surface according to the XRD result (Fig. 1C). As a result, the external film was mainly composed of RE_2O_3 oxide. The secondary phases of scaffold matrix were composed of large flakes mainly containing Y, O, Zr, and the fine dispersed particles with an enrichment of Y, Nd, Gd, Zr. The Y_2O_3 and $Mg_{24}RE_5$ diffraction peaks exhibited in the XRD result of cross section, therefore the flake and particle phases were respectively confirmed as Y_2O_3 and $Mg_{24}RE_5$. Fig. 2A showed the EBSD maps and pole figures of the scaffolds. The scaffold had an average grain size of 7.4 μm and was composed of fine equiaxed grains and coarse columnar grains. A weak grain texture along $< 01\bar{1}0 >$ orientation with an intensity of 4.73 mrd was characterized in the pole figure. As shown in Fig. 2B, the grain sizes with an average value of 7.4 μm were considerably different. The grain sizes were mainly distributed in 5–20 μm with an area fraction of 76.24%. The grain misorientation angles that were greater than 15° accounted for 96.90%, suggesting the recrystallization during HTO was discontinuous (Fig. 2C).

In the compressive test, the yield strength, ultimate strength, and Young's modulus of the scaffolds with HTO were 34.25 ± 0.52 MPa, 57.25 ± 0.41 MPa, and 3.14 ± 0.19 GPa, respectively. Fig. 2D showed the typical compressive stress-strain curve. The scaffolds reached the ultimate compressive strength at about 10% strain. Thereafter, the stress-strain curve exhibits a fluctuation, implying step-by-step crushing. During the compression process, the maximum technical strain (ε_{Te}) was recorded by DIC, as shown in Fig. 2E. When the compression deformation (d) was less than 1 mm, the ε_{Te} exhibited a uniform distribution without severe stress concentration. According to the counted ε_{Te} distribution shown in Fig. 2F, the full-field ε_{Te} of the scaffold revealed a steady increase before the d reached 1 mm. It suggested the scaffold could effectively transform stress and deformation at the early compression process. When the d reached 1.33 mm, significant deformation occurred at the bottom of scaffolds and the stress and deformation could not be transformed. As a result, the full-field ε_{Te} remained unchanged.

3.2. Cell viability and western blot analysis

As displayed in Fig. 3A and B, merged Live/Dead staining and CCK-8 assays showed that the cell viability of the three groups was similarly high on day 1 of culture, and all were close to 100%. The cell line was MC3T3-E1 murine osteoblasts (MC cells). By day 3, further cell proliferation occurred in all groups. On the 7th day after culture, cell viability in all three groups decreased but remained above 75%. From day 1 to day 7, no obvious difference in cell viability was observed among the three groups, only a small number of dead cells formed, indicating the excellent compatibility of scaffold extracts.

Fig. 3C showed the results of the band maps and band grayscale ratios of semi-quantitative OCN and OPN proteins based on Western blot analysis. For OCN, at 1 and 3 days of culture, its semi-quantitative ratio in the 0% extract group was higher than the other two groups ($P < 0.01$ and $P < 0.001$). However, its ratio became the lowest on day 7,
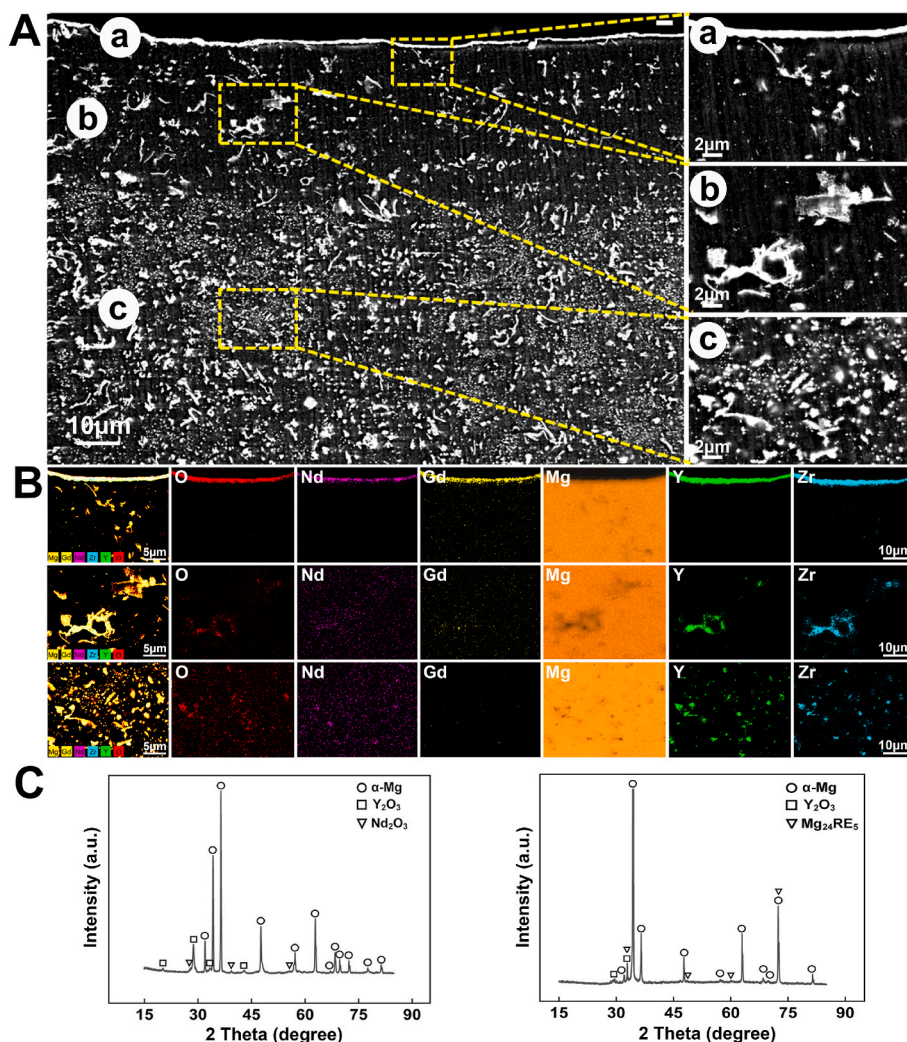
Fig. 1. The surface characteristics for the structure and element of the HTO-modified 3D printed porous WE43 scaffold: (A) SEM images at the corss section; (B) EDS elemtnetal mapping at the cross section; (C) XRD showed the presence of α-Mg, Y_2O_3, Nd_2O_3 and $Mg_{24}RE_5$.

indicating that the scaffold extracts could promote the secretion of OCN by MC cells. For OPN, on the first day of culture, the semi-quantitative ratio in the extract-added groups was significantly higher than that in the 0% extracts group ($P < 0.001$), and a higher extract concentration corresponded to a higher OPN semi-quantitative ratio. This indicated that the extract promoted early OPN secretion. Although the ratio contrast of OPN fluctuated on day 3 of culture, the ratio in groups with 50% and 100% extract became significantly higher again ($P < 0.001$).

3.3. FEA

FEA revealed the stress distribution and concentration among different models, as well as distinguished the von Mises differences of fracture fragments, femoral shafts, plates, screws, cement particles, and scaffolds among all four models. As shown in Fig. 4A a and Fig. 4B a, when the pressure came from the unilateral side, the stress mainly concentrated at the central area of the femoral shafts and plates. At this moment, the highest von Mises values of different parts all appeared in Blank models. The von Mises values of different parts in Cement models were located at a medium level, lower than those of the Blank models and higher than those of the scaffold-implanted groups. Between Scaffold I and Scaffold II groups, an obvious difference in von Mises stress occurred in the aspects of the plate and screws. As shown in Fig. 4A b and Fig. 4B b, when the pressure originated from the overall joint

surface, the stress concentrated at the central area in the same manner. The highest von Mises values of different parts still appeared in the Blank models, but the difference narrowed dramatically. Comparing the two scaffold-implanted groups, the von Mises of fracture fragments, femoral shafts, plates, and screws were lower in the Scaffold I group, but the von Mises of scaffolds did the opposite, being higher in the Scaffold I model. Taken together, when it came to the von Mises of bone-defect filling materials, scaffolds could bear more stress than cement particles under different press modes.

3.4. Gross observations

All rabbits showed various degrees of claudication within 3 weeks after surgery, which was gradually relieved after another 2 weeks. Three rabbits developed incision dehiscence 1 week after surgery and received replacement and supplementation. All the rabbits generally lived in good condition, with a normal mental state and appetite. No obvious signs of inflammation, rejection reaction, or infection were observed in the gross appearance of the harvested femoral samples, indicating good biocompatibility.

3.5. Radiographic examinations: X-rays and Micro-CT scans

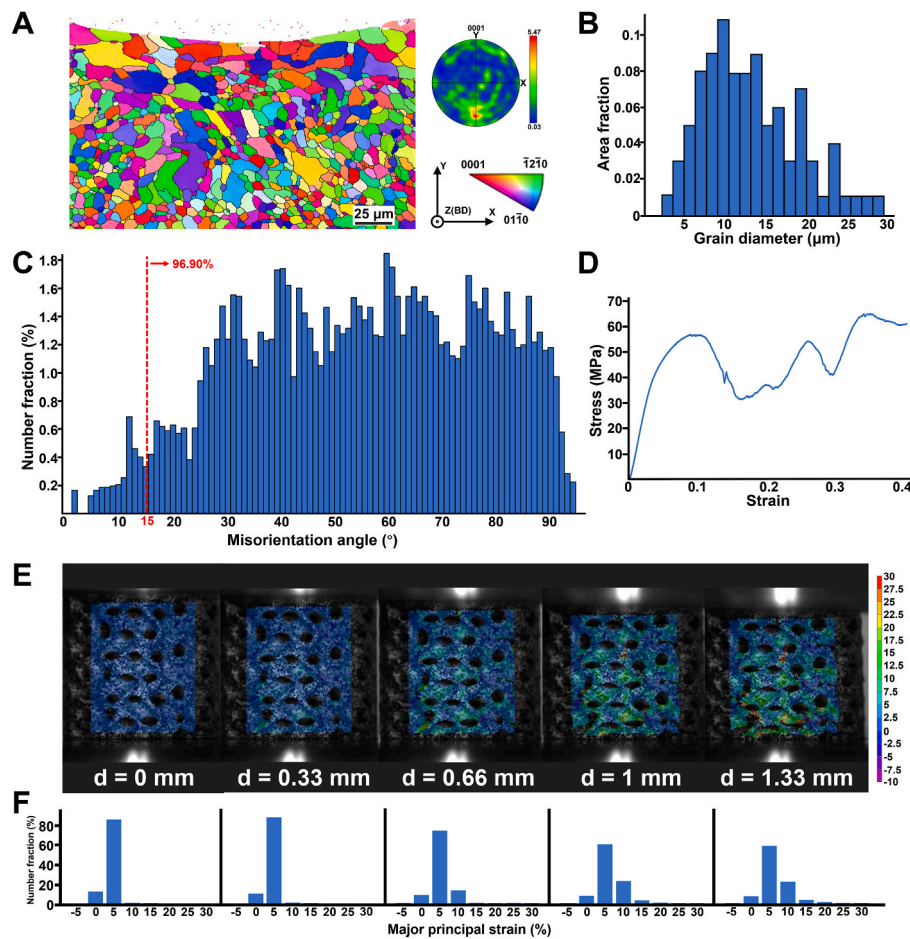As shown in Fig. 5A, serial postoperative X-rays confirmed no

Fig. 2. EBSD and strength analysis for the HTO-modified 3D printed porous WE43 scaffold: (A) EBSD orientation maps displayed the fine equiaxed grains and coarse columnar grains; (B, C) grain sizes and misorientation angles based on EBSD; (D) Stress-strain curve exhibits a step-by-step crushing process; (E, F) DIC images showed the deformation maps of the scaffold surface under changed load, from load bearing, failure load and propagation, significant deformation occurred when the *d* reached 1.33 mm.

obvious loosening or breakage of the screws and plates, and fracture re-displacement, accompanied by blurred fracture lines. The yellow arrows indicated the defect areas, and the red arrows indicated the implanted scaffolds. In the Blank and Cement groups, a low-density space was continuously observed at the bone defect areas from 6 to 48 weeks postoperatively. Meanwhile, cement particles failed to appear at all time nodes. These manifestations confirmed poor bone regeneration and rapid cement degradation. In the Scaffold I group, the entire contour morphology of the scaffold could be clearly distinguished at 6 weeks but disappeared at 12 weeks after surgery. From 12 to 48 weeks, the high-density materials continuously occupied cancellous bone defects, signifying the gradual defect repair process. In the Scaffold II group, the clear contour and porous structure of the scaffolds persisted until 12 weeks after surgery. At 24 and 48 weeks, the bone defects were still filled with high-density materials. Owing to the limited clarity of X-rays, it was difficult to distinguish the detailed compositions of the high-density filling materials in both Scaffold I and Scaffold II groups.

For comparison, Micro-CT scans could display the process of new bone regeneration and scaffold degradation more detailedly. As shown in Fig. 5B, the yellow arrows indicated the defect areas, the red arrows indicated the implanted scaffolds, and the green arrows indicated the newly-regenerated bone. When comparing the Blank and Cement groups, although new bone trabeculae regenerated more in the latter, both groups displayed conspicuously unrepaired defects during the 48-week follow-up periods. Most defect areas remained empty in both groups. In the Scaffold I group, at 6 weeks after surgery, the scaffold had

undergone initial degradation and retained only partially porous structures. Besides, some newly-regenerated bone trabeculae grew along and inside the scaffolds. From 12 to 48 weeks, the porous structures of the scaffolds completely disappeared, and the scaffold residues gradually degraded from large pieces to fine granules. During this process, more bone trabeculae grew inside and formed compact osseointegration with the scaffold residues. In the Scaffold II group, the whole shape and porous structure of scaffolds remained mostly intact 6 weeks after surgery, with only mild degradation occurring in the peripheral area, accompanied by new trabeculae growing surrounding the scaffold. After 12 weeks, the scaffold continued to degrade from the outside towards the inside, accompanied by increased bone regeneration. Several porous structures remained visible. From 24 to 48 weeks, the scaffolds completely lost their porous structure and gradually degraded into granular debris. Similar to what was seen in the Scaffold I group, the newly-regenerated bone trabecula was interwoven together with the scaffold residues, forming tight osseointegration. In comparison, the degradation rate of scaffolds in the Scaffold I group was faster than that in the Scaffold II group, indicating that penetrating screws accelerated the degradation process of the scaffolds to some extent. Micro-CT scans also confirmed that the high-density filling material displayed on the X-ray images was a combination of newly-regenerated bone and scaffold residues.

Combining the serial X-ray and Micro-CT images, the cancellous bone defects in the Blank and Cement groups were not effectively reconstructed and repaired. Notably, because of the rapid degradation
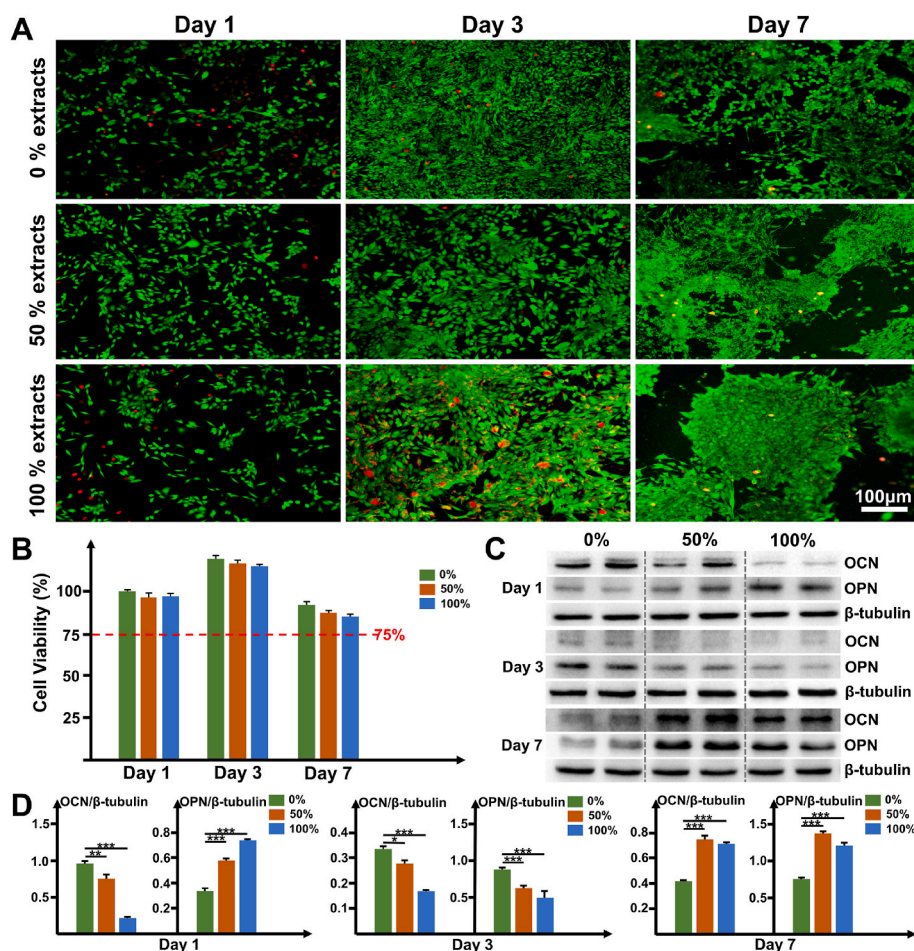
Fig. 3. In vitro cell culture experiment: (A) Live/Dead cells in different concentrations of extracts (0%, 50%, 100%) after 1, 3, and 7 days of culture; (B) Cell viability in different concentrations of extracts; (C, D) Band maps and grayscale ratio of OCN and OPN proteins based on Western blot analysis in different concentrations of extracts (*$P < 0.05$, **$P < 0.01$, ***$P < 0.001$).

rate of cement particles, they failed to promote continuous bone regeneration. The scaffolds could efficiently occupy the defect areas and accelerate bone regeneration. In addition, the newly-regenerated bone could grow inside and form stable osseointegration with the scaffold residues.

3.6. MRI examination

As shown in Fig. 6A, from 6 to 48 weeks postoperatively, there were no obvious signs of inflammatory reactions or infection on the serial MRI images. Moreover, no significant damage was observed in the ligaments, cartilage, or meniscus. As for the quantitative comparison (Fig. 6B), MOCART scores similarly confirmed that periarticular cartilage persistently maintained in good condition during the follow-up period of 48 weeks in all groups, without obvious collapse or defects. The scores of each group were close to 75 points, with no statistically significant differences (P > 0.05).

3.7. Histological analysis

Methylene blue/acid fuchsin staining revealed the progression of scaffold degradation and new bone regeneration more clearly. As shown in Fig. 7, in the Blank and Cement groups, only a small amount of newly-regenerated bone regenerated from 6 to 48 weeks, leaving most of the defect areas vacant. The cement particles were completely degraded 6 weeks after implantation. By contrast, the number of newly-regenerated bone trabeculae was higher in the Cement group. In the Scaffold I group,

the scaffold only retained a slightly porous structure at 6 weeks, accompanied by new bone growing tightly around the periphery and residues of the scaffolds. By 12 weeks, the scaffold had completely lost its porous structure and degraded into dispersed particles. More newly-regenerated bone could be observed around the scaffold residues. From 24 to 48 weeks, a complicated dynamic process involving scaffold degradation and bone regeneration continued, facilitating the self-reconstruction of cancellous bone defects. In the Scaffold II group, 6 weeks after surgery, most of the scaffold remained intact, with only partial degradation at the edges. Some new bone trabeculae regenerated both around the scaffold particles and along the inner wall of the unregenerated scaffold. At 12 weeks, the scaffold partially maintained its porous structure, and more scaffold degradation and bone regeneration occurred with the direction from outside to inside. From 24 to 48 weeks, similar to what was observed in the Scaffold I group, the scaffolds in the Scaffold II group gradually degraded into dispersed particles. Meanwhile, more bone trabeculae regenerated around scaffold residues. The scaffold particles interweaved the newly-regenerated bone to form a tight osseointegration. Comparing the Scaffold I and Scaffold II groups, the degradation rate of scaffolds in the latter group was much slower, which was consistent with the results from the Micro-CT scans. The premature collapse of the whoel scaffold structure caused the growth of new bone to lose directional specificity, whereas the longer retention of the scaffold provided structural crawling support and helped induce new bone to grow thin in the fixed outside-to-inside direction. Even so, these two groups exhibited equal repairing effects on cancellous defects at 48 weeks after surgery, and the defect areas of both groups were filled with
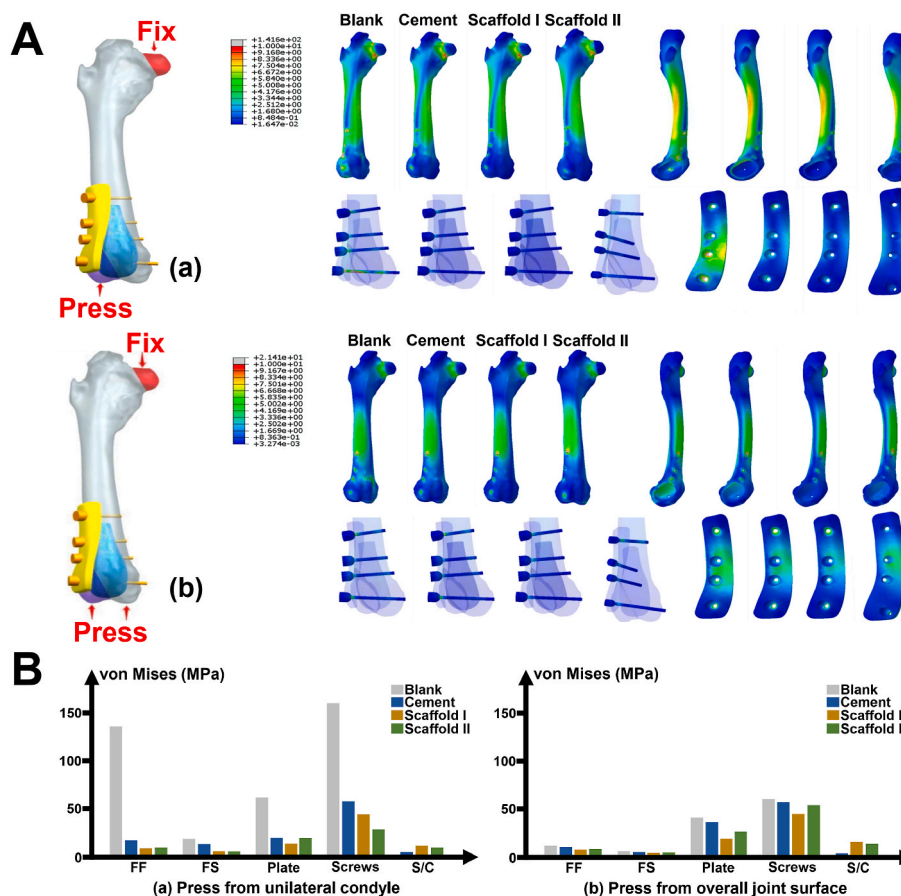
Fig. 4. Biomechanical analysis based on FEA: (A) FEA models displayed the stress distribution of fracture fragments, femoral shafts, plates, screws, cement particles and scaffolds under the press from the distal unilateral condyle (a) or overall joint surface (b). The four models respectively corresponded Blank model, Cement model, Scaffold I model and Scaffold II model from left to right; (B) Von Mises values of different parts under different press patterns (FF: fracture fragments, FS: femoral shaft, S/C: scaffold or cement particles).

the entirety of scaffold particles and newly-regenerated bone, without obvious space.

3.8. Biomechanical experiment

As for the in vitro biomechanical experiment (Fig. 8), at 6 weeks after surgery, the maximum pressure that samples could bear showed no difference between the Blank and Cement groups (P > 0.05), but the result of the Scaffold I group was significantly higher than that of either of them (P < 0.01 or P < 0.05). At 12, 24, and 48 weeks after surgery, the maximum stress-bearing values in the Blank and Cement groups remained similar (P > 0.05), and both were significantly lower than those in the other two scaffold-implanted groups (P < 0.01 or P < 0.05). Comparing the Scaffold I and Scaffold II groups, no obvious difference at all four experimental nodes was observed.

4. Discussion

The advantageous performances of 3D-printed porous WE43 scaffolds for repairing cancellous bone defects were demonstrated in our previous report [14]. With reliable biocompatibility and osteoinduction, the scaffolds successfully promoted the reconstruction of cylindrical bone defects in rabbit models. However, these untreated WE43 scaffolds exhibited rapid degradation, making it difficult to provide lasting and stable biomechanical support in defect areas [14]. Our previous research has reported the effective effect of HTO treatment on the in vitro biodegradation rate [15]. In this research, we further applied the HTO method to optimize the anti-corrosive ability of WE43 scaffolds and

aimed to explore their feasibility and effectiveness for coping the complicated injury type, namely, fractures accompanied by subarticular cancellous bone defects.

Purification, micro-alloying, grain refinement, and coating are alternative treatments for improving the corrosion resistance of Mg alloys [20,21]. Methods such as coating [22] and plasma electrolytic oxidation [23] have been successfully used to mitigate the corrosion of WE43 products. Heat treatment is another alternative method [24], with the advantage that no additional elements or components are added. Because of the different oxidation reactivities of different elements in WE43 alloy, HTO can create element migration and layered structures. Y and Nd are more reactive than Mg, leading to the formation of a dense superficial oxidation layer (mainly comprising Y_2O_3 and Nd_2O_3) and a relatively sparse transition layer. Together, these two layers acted as a barrier and buffer between the external medium and Mg-based substrate, slowing the corrosion of scaffolds. Furthermore, after HTO treatment, the majority of the grains were equiaxed, with an average grain size of 7.4 μm. According to the results from the mechanical test and DIC analysis, the strength and hardness of scaffolds were not significantly weakened after HTO treatment. The Young's modulus of HTO-treated scaffolds (3141.17 ± 188.42 MPa) was very close to that of trabecular bone, which is around 0.44 GPa [25]. This feature results in a uniform stress distribution and reduces the possible stress concentration effects at the interface. Suitable hardness also causes the scaffolds to exhibit good plasticity. These characterizations confirm that HTO-treated WE43 scaffolds are competent for repairing bone defects. In addition, a benefit of using 3D printing technology is that the customized anatomical shape and porous structure endowed these
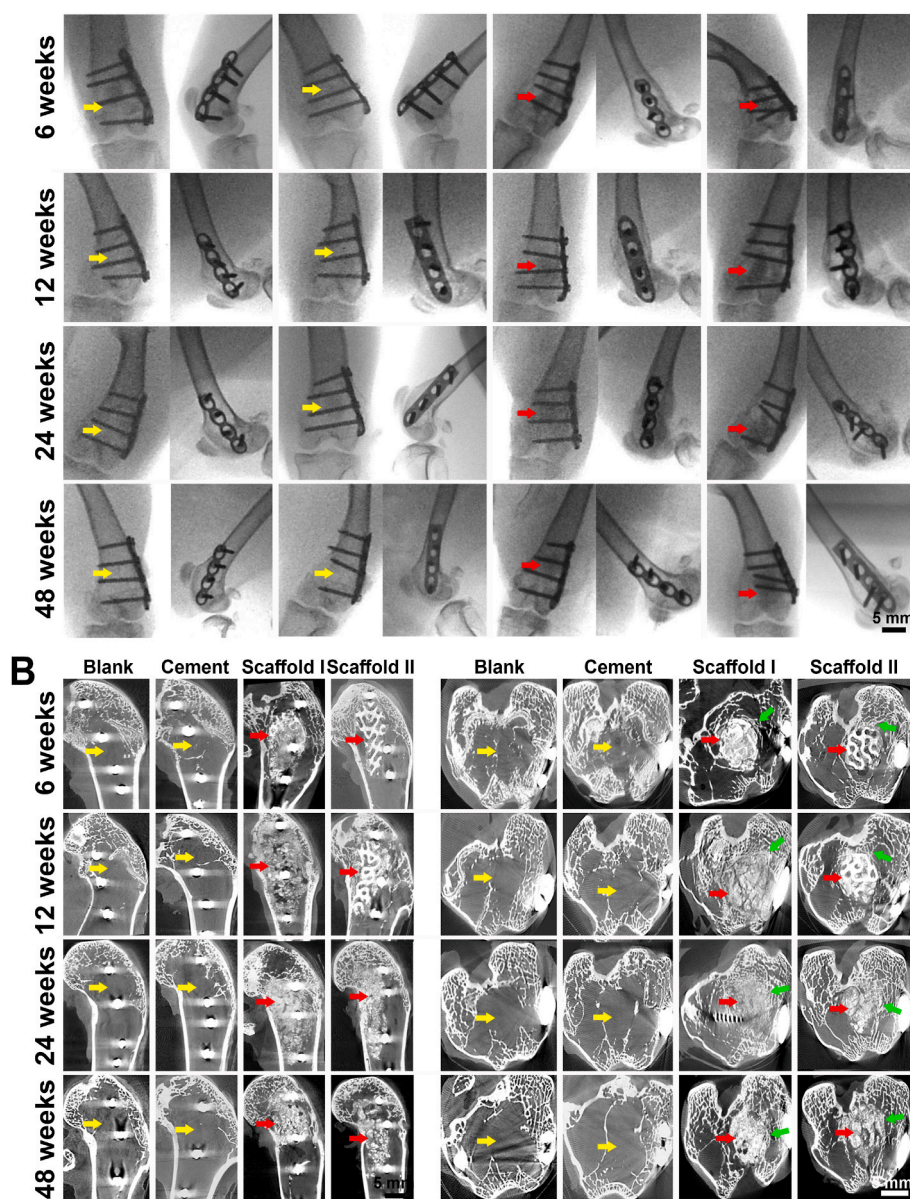
Fig. 5. Results of radiographic examinations: (A) Serial X-rays in anteroposterior and lateral view of different groups at 6, 12, 24 and 48 weeks after surgery; (B) Serial Micro-CT images in sagittal and axial view of different groups at 6, 12, 24 and 48 weeks after surgery (the yellow arrows indicated the defect areas, the red arrows indicated the implanted scaffolds, and the green arrows indicated the newly-regenerated bone.). The results of X-rays, Micro-CTs, MRIs, and histological analysis were obtained from the same rabbit models.

scaffolds with the ability to repair irregular periarticular cancellous bone defects. Under normal physiological conditions, trabecular bone is an anisotropic and porous composite and scaffolds with a porosity comparable to that of trabecular bone (70%–90%) can enhance cell viability and promote bone ingrowth [26,27]. Zhang et al. [28] recommended pore size of 600–700 μm and porosity of close to 70% could contribute to osteogenic activity and new bone formation, which is consistent with the porous parameters of our scaffolds.

Although implants composed of WE43 alloy have been safely used in clinical practice for many years, it is still vital to determine the cytotoxicity and biocompatibility of HTO-treated scaffolds, because thermal oxidation changes the inherent element distribution. According to our cell experiment, MC cells exhibited satisfactory proliferative activity in a medium containing different concentrations of scaffold extracts (50% and 100%), and more than 75% survived after 7 days of culture, without any obvious inhibition. The corresponding cell viability was not significantly different from that in the medium without the scaffold extract. In

subsequent animal experiments, the absence of any reverse response further confirmed the excellent biocompatibility of HTO-treated scaffolds, without toxic, inflammatory, rejective, or allergic reactions. These results indicated that the satisfactory biocompatibility fo WE43 scaffolds were disrupted by HTO treatment, and the scaffolds could be used for repairing *in vivo* bone defects. Similarly, Torroni et al. [24] substantiated good biocompatibility of heat-treated WE43 samples in a cranial sheep model.

Before applying the scaffolds for *in vivo* experiment, we used FEA to determine the effects of different bone-filling materials and fixation modes on mechanical distribution. Regardless of whether the press came from the unilateral side or the overall surface, the von Mises values of fracture fragments, femoral shafts, plates, and screws were all significantly lower than those in the Blank and Cement models. This suggests that the implantation of anatomical WE43 scaffolds can more effectively support the articular surfaces and assist in stress sharing, thereby reducing the stress concentration on the skeletal structure, plates, and
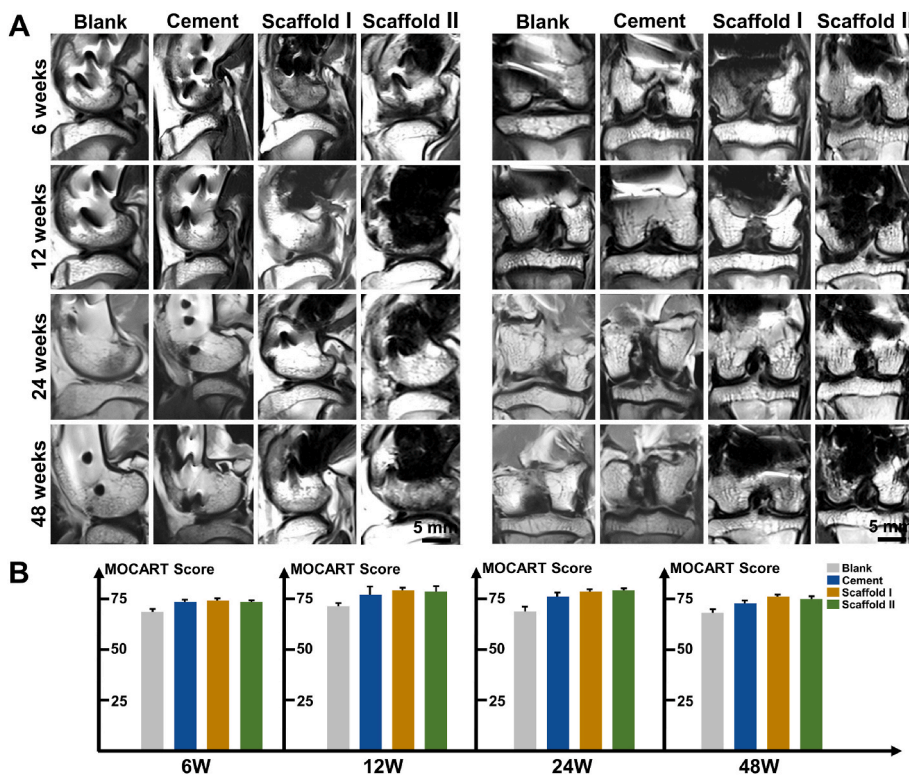
Fig. 6. Results of MRI examinations: (A) Serial MRI images in sagittal and coronal view of different groups at 6, 12, 24 and 48 weeks after surgery; (B) MOCART scores of different groups at 6, 12, 24 and 48 weeks after surgery. The results of X-rays, Micro-CTs, MRIs, and histological analysis were obtained from the same rabbit models.
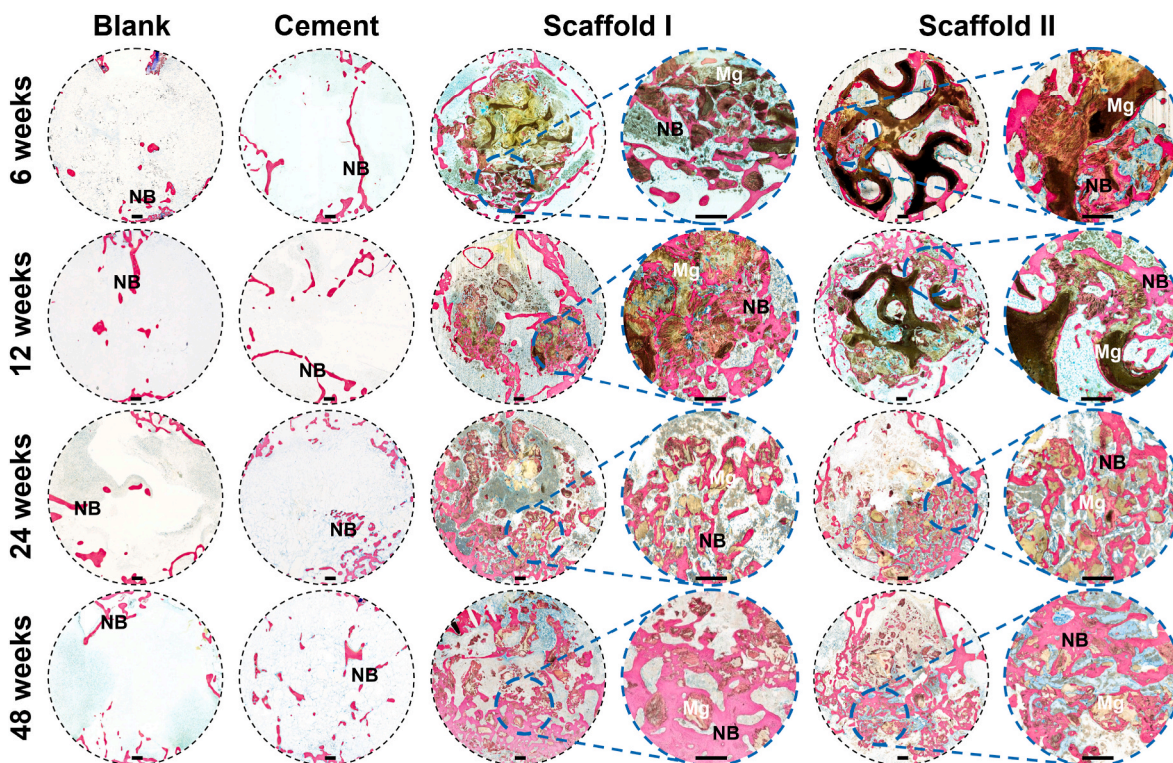

Fig. 7. Results of histological analysis: Methylene blue/acid fuchsin staining exhibited the progression of new bone regeneration and scaffold degradation (Mg: 3D printed WE43 scaffolds; NB: newly-regenerated bone; bar = 0.5 mm). The results of X-rays, Micro-CTs, MRIs, and histological analysis were obtained from the same rabbit models.
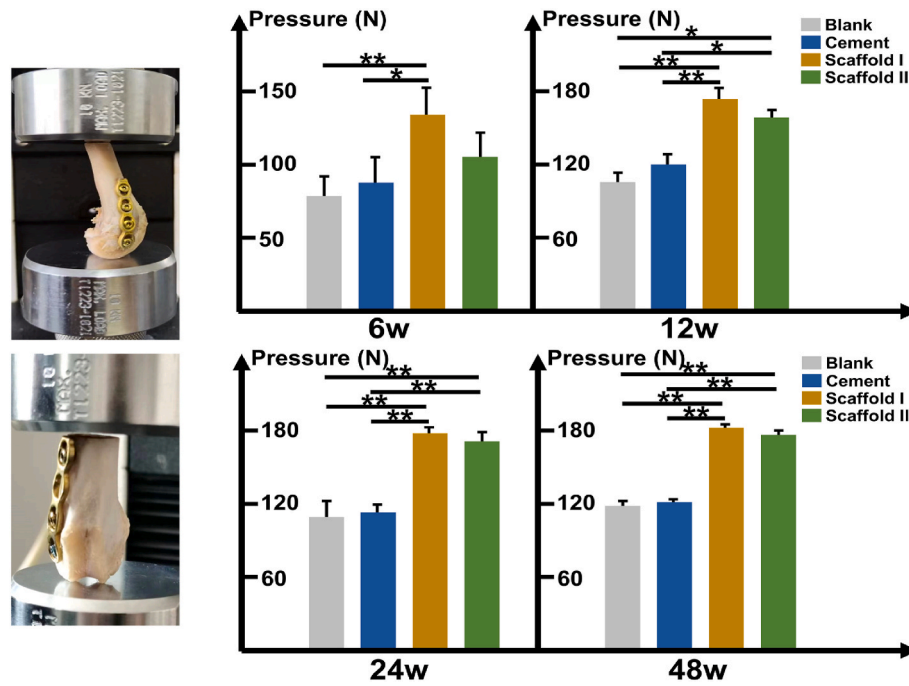
Fig. 8. In vitro biomechanical experiment was accomplished by compressing the harvested samples in axial. During the compression process, we recorded the maximum bearing load through a load-displacement curve. The differences in maximum pressures were statistically analyzed among the four groups at 6, 12, 24 and 48 weeks after surgery (*$P < 0.05$, **$P < 0.01$).

screws, and decreasing the risk of breakage. Moreover, the ability of bone cement particles to share stress was lower than that of the scaffolds. The loose structure of cement particles made it difficult to form a unified stress conduction entirely, which fails to form a stable support for the articular surface. Comparing the Scaffold I and Scaffold II models, when the screws penetrated the scaffolds, the stress dispersed by scaffolds became relatively higher, and the stress on the plates and screws was correspondingly reduced. Hence, the fixation mode of screw penetration was relatively more conducive to overall uniform stress conduction. The results of FEA are consistent with commonly accepted clinical views and phenomena. Screw insertion can reduce the micromovement of implants and enhance their local stability, making it a more recommended fixation mode in bone repair. However, the biological effects of different fixation modes still require verification through *in vivo* animal experiments.

Our present study re-confirmed that HTO treatment could enhance the corrosion resistance of 3D-printed porous WE43 scaffolds. As shown by radiographic examinations and histological analysis, if the scaffolds were not penetrated, they were able to maintain the porous structure as long as 12 weeks after implantation. Under normal physiological conditions, 3–4 months are required from callus formation to new bone reconstruction and eventually solid fracture healing to restore skeletal strength [11]. The structural maintenance period of the HTO-treated WE43 scaffolds exactly matched that of the fracture healing cycle. During this period, the implanted scaffolds provided persistent biomechanical support and prevented periarticular fractures from recollapsing before stable healing. In comparison, scaffolds that were penetrated by screws exhibited a faster degradation rate than those that were not, which might be related to the destruction of the complete structure of superficial oxidation and transition layers. After penetration, the Mg-rich basal layer could come into direct contact with the surrounding body fluids, resulting in rapid corrosion reactions. Moreover, the galvanic corrosion might generate after the contact of WE43 scaffolds and titanium alloy screws, thereby accelerating the degradation of the scaffolds. Even so, the penetrated HTO-treated scaffolds maintained partially porous structures for more than 6 weeks, which was longer than that before HTO treatment, which was less than 4 weeks [14].

According to Micro-CT and histological images, the slower degradation of scaffolds also led to a significant reduction in locally aggregated H_2 cavities. Research has shown that controlling H_2 accumulation during Mg degradation is a critical step in making implants more suitable for the application, as an excessive amount of H_2 gas might disturb bone healing [24]. There was a certain divergence between the results from animal experiments and FEA. From the perspective of the *in vivo* corrosion resistance, it was more advantageous for screws non-penetration. This phenomenon made it worthwhile to further explore the optimal fixation mode of WE43 scaffolds in bone.

The intrinsic osteoinduction ability of WE43 alloy was also not influenced by HTO treatment, which was proved by unitive results at the cellular and animal levels. First, Western blot analysis confirmed that the WE43 scaffold extracts could promote MC cells to secrete OCN and OPN proteins. These two proteins are important bone markers that regulate bone formation [29,30], and participate in up-regulating mineral deposition. Second, combining the serial Micro-CT and histological images, new bone was observed to continuously regenerate around the scaffolds in the defect areas and the number of new trabeculae exceeded those in the Blank and Cement groups. Large-scale irregular cancellous bone defects have outrun the skeletal self-repairing capability, and cement particles were also difficult to persist osteoinduction due to their rapid degradation. In the scaffold-implanted groups, newly-regenerated bones and scaffold residues gradually underwent an interwoven osseointegration. During osteogenesis, Mg ions can regulate the expression of genes and proteins that activate multiple signaling pathways related to osteogenesis [31], increase the expression levels of the angiogenic biomarkers vascular endothelial growth factor, and endothelial nitric oxide synthase [32], and inhibit osteoclast activity [31]. Mg ions can play a regulating role in bone microenvironment and promote bone regeneration continuously [33,34]. Based on the present study, it should be noted that different degradation rates of scaffolds could affect the early growth patterns of new bone trabeculae. The porous structures of scaffolds provided a three-dimensional space for cell adhesion and ingrowth, thereby inducing new bone growth from the outside to the inside. While the degraded scaffolds could only promote new bone growth around their residues, failing to make it follow a fixed

direction. This phenomenon highlighted another obvious advantage of the relatively longer retention time of scaffolds in bone defects, in addition to providing longer mechanical support.

Numerous studies have confirmed that the simultaneous repair of bone and cartilage damage plays a crucial role in preventing the occurrence of osteoarthritis [35,36]. In this study, MRI images demonstrated satisfactory anatomical morphology of articular cartilage, ligaments, and meniscus, without significant degeneration or damage. According to the MOCART scores, there was no significant quantitative difference in cartilage repair between different groups, and all reached a good level close to 75 points. Together concerning the discrepant performance of new bone regeneration in different animal groups, the scaffolds possessed greater advantages for preventing traumatic osteoarthritis thanks to much denser new bone growth. For fractures with simultaneous bone and cartilage damage, the implantation of 3D-printed WE43 scaffold fully play its supporting and osteogenic role.

The ultimate goal of the surgical treatment of periarticular fractures with cancellous defects is to restore the weight-bearing ability of joints. Continuous in vitro biomechanical experiments in this study confirmed that the specimens were unable to bear a large load when the cancellous bone defects were not treated or only filled with bone cement particles, and their maximum load-bearing values were significantly lower than those of the specimens with scaffold filling from 6 to 24 weeks ($P < 0.05$ or $P < 0.01$). The scaffolds could induce abundant bone trabeculae to gradually grow inside the cancellous defects, and the osseointegration could provide stable mechanical support towards the articular surface so that the fractured fragments would not displace easily under pressure. When comparing the Scaffold I and Scaffold II groups, regardless of whether the scaffolds were penetrated by screws, there were no statistically significant differences in the maximum load-bearing values of the specimens ($P > 0.05$). This differed from the phenomenon derived from the FEA simulation in that different fixation patterns of scaffolds could affect the entire stress distribution. In actual animal applications, even if the scaffolds were not penetrated, the newly-regenerated bone trabeculae could act as the structural connecting bridge and stress conduction bond between the scaffolds and skeletal structure, serving as a stable integrated "bone-plate-screw-scaffold" structure. Both scaffold fixation modes could meet the actual practical requirements for repairing periarticular fractures accompanied by cancellous bone defects.

5. Conclusions

HTO-treated 3D printed porous WE43 scaffolds possessed sufficiently good structural and mechanical characteristics, and did not cause cytotoxicity or biological rejection. Their biodegradation rate was also significantly slowed down. When these scaffolds were applied to repair periarticular irregular cancellous bone defects accompanied by a split fracture, they could prominently promote the regeneration of new bone and facilitate the normal healing of damaged bone and cartilage, ultimately restoring the weight-bearing capacity of the articular skeletal structure. These superior performances of the HTO-treated 3D printed porous WE43 scaffolds make them promising candidates for clinical applications. Notably, screw penetration of the HTO-treated scaffolds weakened their *in vivo* corrosion resistance, thereby restricting them from providing longer biomechanical support and pore structures for cell growth. In future studies, we will further reduce the adverse impact of screw penetration on scaffold degradation, making these scaffolds more adaptable to various complex trauma types in clinical settings.

Ethics approval and consent to participate

The experimental protocol was established were carried out in accordance with the guidelines of Good Laboratory Practices regulation and were approved by the Ethical Committee of Laboratory Animal Science Research (No. A2020404).

CRediT authorship contribution statement

Bingchuan Liu: Conceptualization, Investigation, Data curation, Writing – original draft. **Jinge Liu:** Investigation, Data curation, Writing – original draft. **Chaoxin Wang:** Investigation, Data curation. **Zhengguang Wang:** Investigation. **Shuyuan Min:** Investigation. **Caimei Wang:** Resources. **Yufeng Zheng:** Supervision, Resources, Writing – review & editing. **Peng Wen:** Supervision, Resources, Writing – review & editing. **Yun Tian:** Supervision, Resources, Writing – review & editing.

Conflict of interest

The authors declare that they have no competing financial interests or relationships that could influence the work.

Acknowledgements

Appendix A. Supplementary data

Supplementary data to this article can be found online at https://doi.org/10.1016/j.bioactmat.2023.09.016.

References

[1] M. Hartwich, J. Lans, J.B. Jupiter, R. Babst, P. Regazzoni, A.F. Dell'Oca, Joint depression in tibial plateau fractures: to bone graft or not to bone graft? Injury S0020–1383 (23) (2023 Mar 2) https://doi.org/10.1016/j.injury.2023.02.050, 00184-5.

[2] A. Hofmann, S. Gorbulev, T. Guehring, A.P. Schulz, R. Schupfner, M. Raschke, S. Huber-Wagner, P.M. Rommens, CERTiFy Study Group, Autologous iliac bone graft compared with biphasic hydroxyapatite and calcium sulfate cement for the treatment of bone defects in tibial plateau fractures: a prospective, randomized, open-label, multicenter study, J Bone Joint Surg Am 102 (3) (2020 Feb 5) 179–193, https://doi.org/10.2106/JBJS.19.00680.

[3] H. Zhang, S. Wu, W. Chen, Y. Hu, Z. Geng, J. Su, Bone/cartilage targeted hydrogel: strategies and applications, Bioact. Mater. 23 (2022 Nov 11) 156–169, https://doi.org/10.1016/j.bioactmat.2022.10.028.

[4] M.E.V. Barreto, R.P. Medeiros, A. Shearer, M.V.L. Fook, M. Montazerian, J. C. Mauro, Gelatin and bioactive glass composites for tissue engineering: a review, J. Funct. Biomater. 14 (1) (2022 Dec 31) 23, https://doi.org/10.3390/jfb14010023.

[5] H. Yu, H. Liu, Y. Shen, Q. Ao, Synthetic biodegradable polymer materials in the repair of tumor-associated bone defects, Front. Bioeng. Biotechnol. 11 (2023 Feb 16), 1096525, https://doi.org/10.3389/fbioe.2023.1096525.

[6] I. Antoniac, V. Manescu Paltanea, G. Paltanea, A. Antoniac, I.V. Nemoianu, M. I. Petrescu, H. Dura, A.D. Bodog, Additive manufactured magnesium-based scaffolds for tissue engineering, Materials 15 (23) (2022 Dec 6) 8693, https://doi.org/10.3390/ma15238693.

[7] B. Liu, G. Hou, Z. Yang, X. Li, Y. Zheng, P. Wen, Z. Liu, F. Zhou, Y. Tian, Repair of critical diaphyseal defects of lower limbs by 3D printed porous Ti6Al4V scaffolds without additional bone grafting: a prospective clinical study, J. Mater. Sci. Mater. Med. 33 (9) (2022 Sep 14) 64, https://doi.org/10.1007/s10856-022-06685-0.

[8] B. Liu, X. Li, W. Qiu, Z. Liu, F. Zhou, Y. Zheng, P. Wen, Y. Tian, Mechanical distribution and new bone regeneration after implanting 3D printed prostheses for repairing metaphyseal bone defects: a finite element analysis and prospective clinical study, Front. Bioeng. Biotechnol. 10 (2022 Jun 3), 921545, https://doi.org/10.3389/fbioe.2022.921545.

[9] G. Hou, B. Liu, Y. Tian, Z. Liu, F. Zhou, Reconstruction of ipsilateral femoral and tibial bone defect by 3D printed porous scaffold without bone graft: a case report, JBJS Case Connect 12 (1) (2022 Jan 5), https://doi.org/10.2106/JBJS.CC.20.00592.

[10] M. Nasr Azadani, A. Zahedi, O.K. Bowoto, B.I. Oladapo, A review of current challenges and prospects of magnesium and its alloy for bone implant applications, Prog Biomater 11 (1) (2022 Mar) 1–26, https://doi.org/10.1007/s40204-022-00182-x.

[11] Y. Lu, S. Deshmukh, I. Jones, Y.L. Chiu, Biodegradable magnesium alloys for orthopaedic applications, Biomater Transl 2 (3) (2021 Sep 28) 214–235, https://doi.org/10.12336/biomatertransl.2021.03.005.

[12] C. Plaass, C. von Falck, S. Ettinger, L. Sonnow, F. Calderone, A. Weizbauer, J. Reifenrath, L. Claassen, H. Waizy, K. Daniilidis, C. Stukenborg-Colsman,

H. Windhagen, Bioabsorbable magnesium versus standard titanium compression screws for fixation of distal metatarsal osteotomies - 3 year results of a randomized clinical trial, J. Orthop. Sci. 23 (2) (2018 Mar) 321–327, https://doi.org/10.1016/j.jos.2017.11.005.

[13] M. Haude, H. Ince, A. Abizaid, R. Toelg, P.A. Lemos, C. von Birgelen, E. H. Christiansen, W. Wijns, F.J. Neumann, C. Kaiser, E. Eeckhout, S.T. Lim, J. Escaned, H.M. Garcia-Garcia, R. Waksman, Safety and performance of the second-generation drug-eluting absorbable metal scaffold in patients with de-novo coronary artery lesions (BIOSOLVE-II): 6 month results of a prospective, multicentre, non-randomised, first-in-man trial, Lancet 387 (10013) (2016 Jan 2) 31–39, https://doi.org/10.1016/S0140-6736(15)00447-X.

[14] J. Liu, B. Liu, S. Min, B. Yin, B. Peng, Z. Yu, C. Wang, X. Ma, P. Wen, Y. Tian, Y. Zheng, Biodegradable magnesium alloy WE43 porous scaffolds fabricated by laser powder bed fusion for orthopedic applications: process optimization, in vitro and in vivo investigation, Bioact. Mater. 16 (2022 Feb 24) 301–319, https://doi.org/10.1016/j.bioactmat.2022.02.020.

[15] J. Liu, B. Yin, F. Song, et al., Improving corrosion resistance of additively manufactured WE43 magnesium alloy by high temperature oxidation for biodegradable applications, JMA (2022), https://doi.org/10.1016/j.jma.2022.08.009.

[16] S. Amukarimi, M. Mozafari, Biodegradable magnesium biomaterials-road to the clinic, Bioengineering (Basel) 9 (3) (2022 Mar 5) 107, https://doi.org/10.3390/bioengineering9030107.

[17] Z. Wang, B. Liu, B. Yin, Y. Zheng, Y. Tian, P. Wen, Comprehensive review of additively manufactured biodegradable magnesium implants for repairing bone defects from biomechanical and biodegradable perspectives, Front. Chem. 10 (2022 Nov 29) 1066103, https://doi.org/10.3389/fchem.2022.1066103.

[18] E.G. Meinberg, J. Agel, C.S. Roberts, M.D. Karam, J.F. Kellam, Fracture and dislocation classification compendium-2018, J. Orthop. Trauma 32 (Suppl 1) (2018 Jan) S1–S170, https://doi.org/10.1097/BOT.0000000000001063.

[19] S. Marlovits, P. Singer, P. Zeller, I. Mandl, J. Haller, S. Trattnig, Magnetic resonance observation of cartilage repair tissue (MOCART) for the evaluation of autologous chondrocyte transplantation: determination of interobserver variability and correlation to clinical outcome after 2 years, Eur. J. Radiol. 57 (1) (2006 Jan) 16–23, https://doi.org/10.1016/j.ejrad.2005.08.007.

[20] L. Wang, J. He, J. Yu, S. Arthanari, H. Lee, H. Zhang, L. Lu, G. Huang, B. Xing, H. Wang, K.S. Shin, Review: degradable magnesium corrosion control for implant applications, Materials 15 (18) (2022 Sep 6) 6197, https://doi.org/10.3390/ma15186197.

[21] Q. Wang, W. Wang, Y. Li, W. Li, L. Tan, K. Yang, Biofunctional magnesium coating of implant materials by physical vapour deposition, Biomater Transl 2 (3) (2021 Sep 28) 248–256, https://doi.org/10.12336/biomatertransl.2021.03.007.

[22] J. Li, J. Li, N. He, Q. Fu, M. Feng, Q. Li, Q. Wang, X. Liu, S. Xiao, W. Jin, Z. Yu, P. K. Chu, In situ growth of Ca-Zn-P coatings on the Zn-pretreated WE43 Mg alloy to mitigate corrosion and enhance cytocompatibility, Colloids Surf. B Biointerfaces 218 (2022 Oct), 112798, https://doi.org/10.1016/j.colsurfb.2022.112798.

[23] W. Ali, M. Echeverry-Rendón, G. Dominguez, K. van Gaalen, A. Kopp, C. González, J. Llorca, Bioabsorbable WE43 Mg alloy wires modified by continuous plasma electrolytic oxidation for implant applications. Part II: degradation and biological performance, Biomater. Adv. 147 (2023 Apr), 213325, https://doi.org/10.1016/j.bioadv.2023.213325.

[24] A. Torroni, C. Xiang, L. Witek, E.D. Rodriguez, P.G. Coelho, N. Gupta, Biocompatibility and degradation properties of WE43 Mg alloys with and without heat treatment: in vivo evaluation and comparison in a cranial bone sheep model, J. Cranio-Maxillo-Fac. Surg. 45 (12) (2017 Dec) 2075–2083, https://doi.org/10.1016/j.jcms.2017.09.016.

[25] X. Wang, S. Xu, S. Zhou, W. Xu, M. Leary, P. Choong, M. Qian, M. Brandt, Y.M. Xie, Topological design and additive manufacturing of porous metals for bone scaffolds and orthopaedic implants: a review, Biomaterials 83 (2016 Mar) 127–141, https://doi.org/10.1016/j.biomaterials.2016.01.012.

[26] K. Kapat, P.K. Srivas, A.P. Rameshbabu, P.P. Maity, S. Jana, J. Dutta, P. Majumdar, D. Chakrabarti, S. Dhara, Influence of porosity and pore-size distribution in Ti6Al4 V foam on physicomechanical properties, osteogenesis, and quantitative validation of bone ingrowth by micro-computed tomography, ACS Appl. Mater. Interfaces 9 (45) (2017 Nov 15) 39235–39248, https://doi.org/10.1021/acsami.7b13960.

[27] Analysis of Factors Influencing Bone Ingrowth into Three-Dimensional Printed Porous Metal Scaffolds: A Review.

[28] Y. Zhang, N. Sun, M. Zhu, Q. Qiu, P. Zhao, C. Zheng, Q. Bai, Q. Zeng, T. Lu, The contribution of pore size and porosity of 3D printed porous titanium scaffolds to osteogenesis, Biomater. Adv. 133 (2022 Feb), 112651, https://doi.org/10.1016/j.msec.2022.112651.

[29] T. Komori, Functions of osteocalcin in bone, pancreas, testis, and muscle, Int. J. Mol. Sci. 21 (20) (2020 Oct 12) 7513, https://doi.org/10.3390/ijms21207513.

[30] R.J. Bai, Y.S. Li, F.J. Zhang, Osteopontin, a bridge links osteoarthritis and osteoporosis, Front. Endocrinol. 13 (2022 Oct 28), 1012508, https://doi.org/10.3389/fendo.2022.1012508.

[31] Z. Shan, X. Xie, X. Wu, S. Zhuang, C. Zhang, Development of degradable magnesium-based metal implants and their function in promoting bone metabolism (A review), J Orthop Translat 36 (2022 Oct 8) 184–193, https://doi.org/10.1016/j.jot.2022.09.013.

[32] Y. Gu, J. Zhang, X. Zhang, G. Liang, T. Xu, W. Niu, Three-dimensional printed Mg-doped β-TCP bone tissue engineering scaffolds: effects of magnesium ion concentration on osteogenesis and angiogenesis in vitro, Tissue Eng Regen Med 16 (4) (2019 Jun 17) 415–429, https://doi.org/10.1007/s13770-019-00192-0.

[33] S. Chen, X. Chen, Z. Geng, J. Su, The horizon of bone organoid: a perspective on construction and application, Bioact. Mater. 18 (2022 Feb 5) 15–25, https://doi.org/10.1016/j.bioactmat.2022.01.048.

[34] S. Hao, M. Wang, Z. Yin, Y. Jing, L. Bai, J. Su, Microenvironment-targeted strategy steers advanced bone regeneration, Mater Today Bio 22 (2023 Jul 21), 100741, https://doi.org/10.1016/j.mtbio.2023.100741.

[35] S.E. Doyle, F. Snow, S. Duchi, C.D. O'Connell, C. Onofrillo, C. Di Bella, E. Pirogova, 3D printed multiphasic scaffolds for osteochondral repair: challenges and opportunities, Int. J. Mol. Sci. 22 (22) (2021 Nov 17), 12420, https://doi.org/10.3390/ijms222212420.

[36] L. Yu, S. Cavelier, B. Hannon, M. Wei, Recent development in multizonal scaffolds for osteochondral regeneration, Bioact. Mater. 25 (2023 Feb 2) 122–159, https://doi.org/10.1016/j.bioactmat.2023.01.012.